

Time-series analysis of vibrational nuclear wave-packet dynamics in D_2^+

Uwe Thumm,^{1,2,*} Thomas Niederhausen,¹ and Bernold Feuerstein²

¹James R. Macdonald Laboratory, Kansas State University, Manhattan, Kansas 66506-2604, USA

²Max-Planck-Institut für Kernphysik, D-69029 Heidelberg, Germany

(Received 3 December 2007; published 3 June 2008)

We discuss the extent to which measured time-dependent fragment kinetic energy release (KER) spectra and calculated nuclear probability densities can reveal (1) the transition frequencies between stationary vibrational states, (2) the nodal structure of stationary vibrational states, (3) the ground-state adiabatic electronic potential curve of the molecular ion, and (4) the progression of decoherence induced by random interactions with the environment. We illustrate our discussion with numerical simulations for the time-dependent nuclear motion of vibrational wave packets in the D_2^+ molecular ion caused by the ionization of its neutral D_2 parent molecule with an intense pump laser pulse. Based on a harmonic time-series analysis, we suggest a general scheme for the full reconstruction, up to an overall phase factor, of the initial wave packets based on measured KER spectra. We apply this scheme in a numerical simulation for vibrational wave packets in D_2^+ molecular ions and show how this reconstruction allows the clear distinction between commonly assumed stationary vibrational state distributions of the molecular ion following the ionization of D_2 .

DOI: 10.1103/PhysRevA.77.063401

PACS number(s): 42.50.Md, 33.20.Tp, 82.37.Np

I. INTRODUCTION

The anticipated efficient catalysis and control of chemical reactions with laser light has been the motivation for many detailed theoretical and experimental investigations over the past two decades [1–3]. Within the past few years, intense laser pulses with durations below the vibrational period of even small molecules became available, and the time evolution of nuclear wave packets is now routinely imaged in several laboratories world wide [4–11]. The time-dependent nuclear motion is detected by combining a femtosecond pump-probe experiment with the Coulomb explosion (CE) imaging of the molecular fragments [12–17]. In this type of pump-probe experiment, the first (pump) pulse ionizes a neutral molecule and generates a coherent nuclear wave packet in the molecular ion. A second delayed (probe) pulse detects the wave packet at the pump-probe delay time by dissociating or rapidly ionizing the molecular ion. Ionization in the probe pulse leads to nearly instant fragmentation of the molecular ion by CE. By recording the KER of those fragments that were produced by CE as a function of the delay time, the evolution of the coherent (and decohering) nuclear motion can be monitored in great detail, in particular for diatomic molecules [5,6,8,9,11]. Due to their simple structure, the KER following the CE of diatomic molecules can be accurately mapped on a distribution of internuclear distances R at a time immediately preceding ionization thereby allowing for the direct and time-resolved observation of molecular excitation, bond breaking, temporary bond formation, ionization, and vibrational-state-resolved dissociation [9,11,16,18–21]. In contrast to other pump-probe schemes, such as, e.g., “pump-dump” interrogations of molecular potential curves with two-color stimulated Raman scattering [22], and depending on the realization of the probe-ionization step, pump-probe CE imaging provides information about the

nuclear wave packet, simultaneously over a large interval of internuclear distances, as indicated in Fig. 1.

Computationally, small molecules, in particular H_2 , H_2^+ , and their isotopes, have become accessible to realistic numerical modeling and, therefore have bench-marking potential. The comparison with measured KER spectra allows for increasingly severe tests of quantum mechanical wave-packet propagation (WPP) calculations [9,11,16], and, more specifically, for a critical assessment of control protocols suggested by such numerical simulations [23–26]. For example, the coherent nuclear motion in D_2^+ was recently observed over several picoseconds [23] and was found to accurately reproduce theoretically predicted details [16], such as the occurrence of partial and full vibrational revivals after many vibrational periods ($T_{\text{vib}} \approx 22$ fs in D_2^+). Recent experiments with fs laser pulses and WPP calculations show an

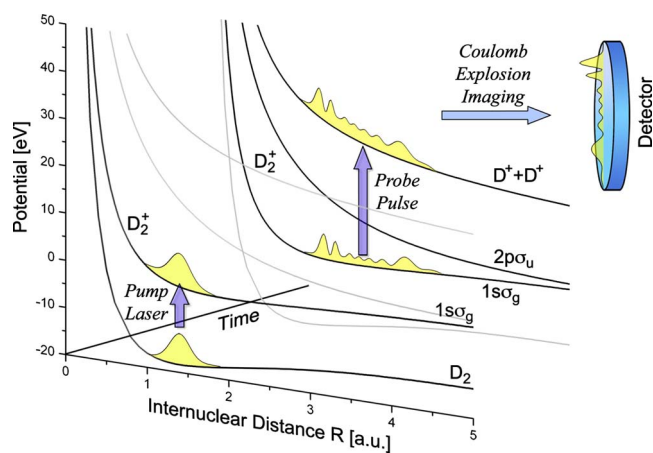


FIG. 1. (Color online) Schematic diagram of the pump-probe setup. A first laser pulse launches a nuclear wave packet on the D_2^+ $1s\sigma_g^+$ potential curve and starts the molecular clock. After a certain delay time, an intense short probe pulse promotes the nuclear wave packet onto the $2D^+$ repulsive $1/R$ Coulomb-explosion curve and allows for the detection of the fragment-kinetic-energy distribution.

*thumm@phys.ksu.edu

increasing amount of control in steering the bound and dissociating motion in molecules by tuning laser pulse parameters (duration, intensity, and shape) or by adding one (or more) control laser pulses in between the pump-probe sequence [9,26,27].

In the present paper, we outline a scheme for probing and reconstructing the dynamics of moving wave packets. The suggested method is general in the sense that it may be applied to the analysis of electronic, rotational and vibrational wave packets. In Sec. II we will illustrate our discussion with reference to the concrete example of laser-excited coherent nuclear vibrational motion in D_2^+ molecular ions. This allows us to numerically simulate the analysis of the primary data provided by pump-probe experiments, pump-probe-delay-dependent KER spectra, and to demonstrate how our scheme reveals information about (1) the beat frequencies between vibrational states, (2) the nodal structure of D_2^+ stationary vibrational states, (3) the ground-state adiabatic electronic potential curve of D_2^+ , (4) light-induced molecular potentials that may allow for the formation of transiently trapped molecular states (so-called “bond-hardening” states), and (5) the coherent stationary vibrational-state composition of the vibrational wave packet in D_2^+ . Before presenting our conclusions, we shall briefly discuss in Sec. III an extension of our scheme for analyzing R -dependent KER data by (6) allowing for the loss of coherence due to random interactions with the environment. Even though our numerical examples are limited to the coherent motion in D_2^+ , our method may be extended to larger molecules and offer a way to quantify the progression of decoherence due to couplings to the experimental environment in polyatomic molecules and systems of interest for application in emerging quantum information technologies. We assume atomic units throughout this work, unless indicated otherwise, and designate the vibrational ground states of D_2 and D_2^+ with the index $\nu=0$ and excited states with $\nu \geq 1$.

II. COHERENT WAVE PACKET DYNAMICS

A. Bound nuclear motion

1. Generation and evolution of nuclear wave packet

In order to efficiently generate a coherent vibrational wave packet in D_2^+ , the pump laser pulse has to satisfy several requirements. Its intensity needs to be sufficiently large to singly ionize the parent D_2 molecule and small enough to avoid instant Coulomb explosion following double ionization. Its pulse length should be short enough for its spectral band width to be of the order of (or larger than) the typical frequency difference of neighboring vibrational states. If two or more stationary vibrational states χ_ν of D_2^+ satisfy this requirement, their coherent superposition

$$\Psi(R,t) = \sum_{\nu=0}^N a_\nu e^{-i\omega_\nu t} \chi_\nu(R) \quad (1)$$

forms a moving wave packet. After the pump pulse has passed, this wave packet freely propagates on the $1s\sigma_g^+$ potential curve of D_2^+ . In the absence of further external inter-

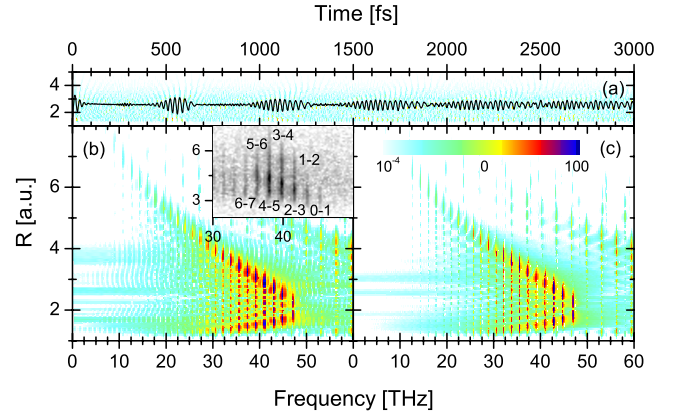


FIG. 2. (Color online) (a) Time evolution of an initial Franck-Condon D_2^+ vibrational packet. Probability density (logarithmic color scale) and expectation value of the internuclear distance $\langle R \rangle$ (thick line). (b),(c) Squared Fourier transform (power spectrum) of the evolution of the probability density as a function of the internuclear distance R , $|\tilde{d}(R, \omega; T)|^2$. The sampling times are $T=3$ ps (b) and 10 ps (c). Inset in (b): First experimental evidence by Feuerstein *et al.* [23] for $T=3$ ps. Hyphenated pairs of quantum numbers indicate the beating stationary vibrational states. All graphs show the beat frequency $f = \omega / (2\pi)$ on the horizontal axis.

actions (and disregarding molecular rotation) it undergoes cycles of dephasing and revivals [10,11,16,27,28] without changing its vibrational-state distribution $\{a_\nu(0) = \langle \chi_\nu | \Psi(R, t=0) \rangle\}$. Its probability density $|\Psi(R, t)|^2$ [Fig. 2(a)] is directly related to the Coulomb explosion image of the measurable time-dependent KER.

D_2^+ vibrational wave packets are generated in the pump laser pulse by ionization of neutral D_2 molecules out of their vibrational (and electronic) ground state. The rate for ionization of the neutral molecule increases rapidly with the internuclear distance R [29], such that the often-used Franck-Condon (FC) approximation provides a rather poor model of the ionization process and is known to generate a vibrational state distribution $\{a_\nu\}$ in D_2^+ that overestimates the population of higher excited vibrational states [30]. In our numerical examples, we model the ionization of D_2 based either on the FC approximation or on molecular Ammosov-Delone-Krainov (ADK) tunneling ionization rates $\Gamma_{\text{ADK}}(R, I)$ [26,31]. The molecular ADK rate is derived from the original rate for tunneling ionization of (one-electron) atoms in a static electric field [32] and owes its dependence on R to the implicit generalization of the atomic ionization potential to the vertical (at a given value of R) energy gap between the adiabatic energies of the neutral diatomic molecule and its daughter molecular ion in their respective ground electronic states. For the remainder of this paper, we will refer to the resulting D_2^+ wave packets as either “FC-wave packets” or “ADK-wave packets.” Similarly, we will address their initial stationary vibrational state distributions $\{a_\nu\}$ as “FC” or “ADK distribution,” respectively.

While within the FC approximation the population of a specific vibrational state ν in D_2^+ is obtained simply by projecting the vibrational ground state of the neutral molecule $\chi_{\nu=0}^{D_2}$ onto χ_ν and thus does not depend on the laser param-

eters, molecular-ADK rates depend on the pump-laser intensity. We note that for arbitrary orientation of the molecule relative to the laser electric field, orientation-dependent molecular ADK rates [33] would be more accurate. However, since the molecular orientation can be determined experimentally [5], we disregard the orientation dependence of molecular ionization. The pump laser is assumed to launch the vibrational wave packet at time $t=0$, thereby starting a “molecular clock.” Including the partial depletion of the initial vibrational state of the D_2 molecule by the pump pulse, we model the nuclear wave function of the neutral molecule after the pump pulse as

$$\chi_{\text{pump}}^{D_2}(R) = \chi_{\nu=0}^{D_2}(R) \exp \left\{ - \int_0^\infty dt \Gamma_{\text{ADK}}[R, I(t)]/2 \right\} \quad (2)$$

and obtain the normalized initial wave packet in D_2^+

$$|\Psi(R, t=0)\rangle = (\chi_{\nu=0}^{D_2} - \chi_{\text{pump}}^{D_2}) / \|\chi_{\nu=0}^{D_2} - \chi_{\text{pump}}^{D_2}\|. \quad (3)$$

The initial vibrational-state distribution $\{a_\nu(0)\}$ changes if the molecular ion interacts with a laser pulse. Allowing for laser-induced Raman transitions between the two lowest adiabatic potential curves in D_2^+ , we switch to a convenient two-component representation of the nuclear wave function and adopt a two-state model for the propagation of the nuclear wave packet

$$|\Psi(t)\rangle = \begin{pmatrix} \chi_g(t) \\ \chi_u(t) \end{pmatrix} \quad (4)$$

on the $1s\sigma_g$ and $2p\sigma_u$ potential curves

$$i \frac{d}{dt} \begin{pmatrix} \chi_g \\ \chi_u \end{pmatrix} = (\hat{T} + \hat{V} + \hat{H}_c) \begin{pmatrix} \chi_g \\ \chi_u \end{pmatrix}. \quad (5)$$

The initial condition for the nuclear wave packet components on the D_2^+ potential curves of gerade and ungerade symmetry [34] are given by

$$\chi_g(R, t) = \sum_{\nu=0}^N a_\nu(0) e^{-i\omega_\nu t} \chi_\nu(R), \quad (6)$$

$$\chi_u(R, t) = 0. \quad (7)$$

The kinetic energy operator $\hat{T} = p^2/(2\mu)$ includes the reduced mass $\mu = 1835$ of the two nuclei. The adiabatic $1s\sigma_g$ and $2p\sigma_u$ electronic potential curves of D_2^+ [34] form the diagonal elements of the potential matrix

$$\hat{V} = \begin{pmatrix} V_g(R) & 0 \\ 0 & V_u(R) \end{pmatrix}. \quad (8)$$

The laser-induced dipole coupling between the gerade and ungerade potential curves in D_2^+ is included in the off-diagonal elements of the coupling operator

$$\hat{H}_c = \begin{pmatrix} -\frac{i}{2} \Gamma_g^{D_2^+}[R, E(t)] & D_{gu}(R)E(t) \\ D_{gu}(R)E(t) & -\frac{i}{2} \Gamma_u^{D_2^+}[R, E(t)] \end{pmatrix} \quad (9)$$

and depends on the electronic dipole moment between the two adiabatic electronic states ψ_g and ψ_u , $D_{gu}(R) = \langle \psi_u | z | \psi_g \rangle$ [35], and the laser electric field $E(t) = E_0(t) \cos \omega t$. The brackets in $\langle \psi_u | z | \psi_g \rangle$ indicate integration over the electronic coordinates x , y , and z , and the laser is assumed to be linearly polarized along the z axis. The diagonal elements in \hat{H}_c include the (isotropic) molecular ADK rates $\Gamma_g^{D_2^+}[R, E(t)]$ and $\Gamma_u^{D_2^+}[R, E(t)]$ for the ionization of D_2^+ out of the $1s\sigma_g$ and $2p\sigma_u$ electronic states [26,31].

2. R-dependent quantum-beat analysis

By subtracting the time-averaged probability density, i.e., the incoherent diagonal term, from $|\Psi(R, t)|^2$, we define

$$d(R, t) \equiv |\Psi(R, t)|^2 - \frac{1}{T} \int_0^T dt |\Psi(R, t)|^2, \quad (10)$$

$$= \sum_{\nu \neq \mu} a_\nu^* a_\mu e^{i\Delta\omega_{\nu,\mu} t} \chi_\nu^*(R) \chi_\mu(R). \quad (11)$$

Harmonic analysis at a fixed value of the internuclear distance R ,

$$\begin{aligned} \tilde{d}(R, \omega; T) &\equiv \frac{1}{\sqrt{2\pi}} \int_0^T dt d(R, t) e^{-i\omega t}, \\ &= \sqrt{2\pi} \sum_{\nu \neq \mu} \tilde{d}_{\nu,\mu}(R, \omega; T), \end{aligned} \quad (12)$$

maps the vibrational transition frequencies $\Delta\omega_{\nu,\mu} = \omega_\mu - \omega_\nu$ onto a series of vertical lines in the graph of $\tilde{d}(R, \omega; T)$ with ω on the horizontal and R on the vertical axis. This is shown in Figs. 2(b) and 2(c) where, since the phase of $\tilde{d}(R, \omega; T)$ is not observable, the squared amplitude (or “power spectrum”) $|\tilde{d}(R, \omega; T)|^2$ is plotted as a function of $f = \omega/(2\pi)$ and R . The individual contributions to the R -dependent spectrum (12) near the quantum-beat frequencies $\Delta\omega_{\nu,\mu}$ are

$$\tilde{d}_{\nu,\mu}(R, \omega; T) \equiv a_\nu^* a_\mu \chi_\nu^*(R) \chi_\mu(R) \delta_T(\Delta\omega_{\nu,\mu} - \omega). \quad (13)$$

The vertical lines are centered at $\Delta\omega_{\nu,\mu}$ and are the better resolved, the larger the sampling time T is. This is demonstrated in Figs. 2(b) and 2(c) where the evolution of a D_2^+ wave packet with an initial FC distribution $\{a_\nu(0)\}$ is frequency-analyzed for $T=3$ and 10 ps, respectively. For sampling times that are long on the vibrational time scale T_{vib} , the complex-valued distribution

TABLE I. Sampling times T with corresponding frequency resolution $\Delta\omega_T$ and energy resolution $\Delta\epsilon_T = \hbar\Delta\omega_{\min}$.

T [ps]	$\Delta\omega_T$ [a.u.]	$\Delta\epsilon_T$ [meV]
0.8	3.7×10^{-4}	10
3	1.0×10^{-4}	2.7
10	3.0×10^{-5}	0.8

$$\delta_T(\Omega) \equiv \frac{1}{2\pi} \int_0^T dt e^{i\Omega t}, \quad (14)$$

$$= \frac{1}{\pi} e^{i\Omega T/2} \frac{\sin(\Omega T/2)}{\Omega} \quad (15)$$

in Eq. (13) approaches the real-valued delta “function” $\delta_T(\Omega) \rightarrow \delta(\Omega)$ up to the irrelevant overall phase factor $e^{i\Omega T/2}$, and $\tilde{d}(R, \omega; T)$ approaches its limit of infinite energy resolution $\tilde{d}(R, \omega; \infty)$. The strength of all vertical lines in the power spectrum is proportional to $|\delta_T(0)|^2 = [T/(2\pi)]^2$. These properties of $\delta_T(\Omega)$ imply that the R -dependent structure in the wave-function product $\chi_\nu^*(R)\chi_\mu(R)$ appears most clearly in the finite-time-Fourier-transformation spectrum $\tilde{d}(R, \omega; T)$ for large sampling times and for $\Omega \approx 0$, i.e., near the beat frequencies $\Delta\omega_{\nu,\mu}$. In order to resolve adjacent beat frequencies in the spectrum (12), the sampling time needs to be sufficiently large to guarantee that

$$\Delta\omega_{\nu,\nu+1} > \Delta\omega_T \equiv \frac{4\pi}{T}. \quad (16)$$

A few examples for the dependence of the frequency resolution in $\tilde{d}(R, \omega; T)$ on T are given in Table I. As the table shows, a sampling time of 800 fs is barely large enough to resolve beats of adjacent stationary vibrational eigenstates in D_2^+ , while they can be resolved for $T \geq 3$ ps.

Each series of vertical lines in $\tilde{d}(R, \omega; T)$ is defined by a specific vibrational gap $\Delta\nu$. Due to the specific anharmonicity of the $1s\sigma_g^+$ potential curve of D_2^+ , lines in the $\Delta\nu=1$ series are ordered as $\Delta\omega_{0,1} > \Delta\omega_{1,2} > \Delta\omega_{2,3} > \dots$. Similarly, the $\Delta\nu=2$ series consists of vertical lines at the beat frequencies $\Delta\omega_{0,2} > \Delta\omega_{1,3} > \Delta\omega_{2,4} > \dots$ in the graph of $\tilde{d}(R, \omega; T)$ versus R and ω [Fig. 3(b)].

Closer inspection of Eq. (12) reveals that the R -dependent structure in each vertical line in $|\tilde{d}(R, \omega; T)|^2$ maps the nodes of the stationary vibrational wave functions [Figs. 2(b) and 2(c)]. The intensities of the lines at $\Delta\omega_{\nu,\mu}$ are proportional to the products $|\chi_\nu^*(R)\chi_\mu(R)|^2$, and each line displays a certain number of nodes which is equal to the sum $\nu+\mu$ of the nodes of the two vibrational states χ_ν and χ_μ . Due to the large overlap of the probability between successive stationary vibrational states in Eq. (12), lines of the $\Delta\nu=1$ series are mapped with the largest intensities, while larger values of $\Delta\nu$ lead to a less intense portrait of the R -dependency in the product $\chi_\nu^*(R)\chi_\mu(R)$ [Figs. 3(b) and 3(c)].

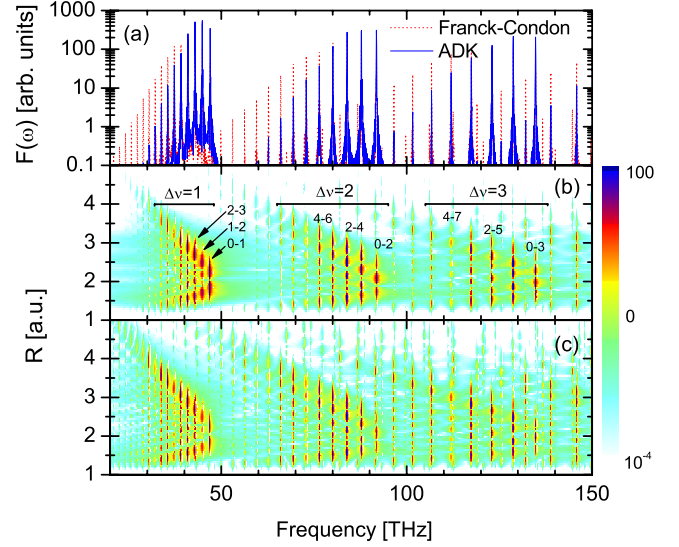


FIG. 3. (Color online) (a) R -integrated line strength $F(\omega)$ (see text). (b),(c) $|\tilde{d}(R, \omega; T)|^2$ for $T=10$ ps and for the three series of beat frequencies with $\Delta\nu=1, 2$, and 3. (b) initial D_2^+ wave packet based on ADK-ionization rates. Hyphenated pairs of numbers indicate beat frequencies for a few selected vibrational states. (c) Initial Franck-Condon wave packet in D_2^+ . The horizontal axis shows the beat frequency $f = \omega / (2\pi)$.

3. Imaging molecular potential curves

Ultrashort pump pulses generate vibrational wave packets as a linear combination of many bound stationary vibrational states $\{\chi_\nu\}$. Since each wave function $\chi_\nu(R)$ retraces the interface between classically allowed and forbidden internuclear distances by the onset of the exponentially decaying probability density, R -dependent power spectra offer the possibility to map the shape of molecular potential curves. Indeed, our simulations in Figs. 2(b) and 2(c) show contours that resemble the shape of the $1s\sigma_g^+$ potential curve of D_2^+ .

For each vibrational gap $\Delta\nu$ a separate contour is obtained. This is shown in Fig. 3 which contains the power spectrum for a sampling time of 10 ps for initial D_2^+ wave packets that are based either on molecular ADK-ionization rates for D_2 [Fig. 3(b)] or on the FC principle [Fig. 3(c)]. The initial ADK distribution in Fig. 3(b) is calculated for a Gaussian 800 nm pump pulse with a duration of 6 fs FWHM and an intensity of 10^{14} W/cm². Series of quantum beats for different values of $\Delta\nu$ remain distinguishable. Within each series, the individual frequencies are clearly separated. Integration over R at fixed beat frequencies yields the distribution of line strengths $F(\omega)$ in Fig. 3(a). For larger $\Delta\nu$ these contours are stretched over a wider range in beat frequencies. Figures 3(b) and 3(c) display the $\Delta\nu=1, 2$, and 3 quantum beat series together with a background of “intruder” lines from the $\Delta\nu \geq 3$ series.

It is important to note that these contour lines show frequency differences between vibrational states rather than frequencies (or energies). The resemblance of the contour lines in Figs. 2 and 3 with the actual $1s\sigma_g^+$ adiabatic molecular potential curve of D_2^+ is a signature of the anharmonic character of the potential and to some degree fortuitous. This

becomes immediately obvious by considering a harmonic potential curve. Since all energy eigenvalues $(n+0.5)\omega_{\text{HO}}$ of the harmonic oscillator are equally spaced, all quantum beat frequencies for two levels of a given $\Delta\nu$ series collapse on a single line at frequency $\Delta\nu\omega_{\text{HO}}$ in the beat spectrum. In order to obtain the actual molecular potential curves, the beat frequencies, together with all corresponding vertical lines of the R -dependent quantum beat spectrum, need to be mapped onto the sequence $\{\omega_{\nu}^{\text{recon}}\}$ of the reconstructed stationary vibrational state energies according to

$$\omega_{\nu}^{\text{recon}} = \sum_{\mu=1}^{\nu} \Delta\omega_{\mu,\mu-1} + \omega_{\text{ref}}. \quad (17)$$

This simple transformation provides the molecular potential energy curve up to an undetermined reference energy ω_{ref} .

4. Amplitude reconstruction

In order to reconstruct the initial vibrational wave packet, the complex expansion coefficients $\{a_{\nu}(0), \nu=1, \dots, N\}$ in Eq. (1) need to be obtained based on the information contained in the KER spectrum. Each coefficient $a_{\nu} = |a_{\nu}|e^{i\phi_{\nu}}$ is determined by its amplitude $|a_{\nu}|$ and phase ϕ_{ν} . In this subsection we will describe how the amplitudes $|a_{\nu}|$ can be extracted from the KER spectra.

While the reconstruction of the expansion coefficients (up to an undetermined global phase factor) could be achieved by a direct fit of the probability density that is given by the squared absolute value of Eq. (1) to the corresponding CE-imaged probability density derived from a measured KER spectrum, the Fourier-transformation method we going to apply appears to be more accurate for the following reasons. (i) A direct fit would be nonlinear since the probability density is quadratic in the expansion coefficients. Therefore, starting with the definition of a chi-squared merit function, the best fit to the set of N complex amplitudes $\{a_k\}$ had to be determined iteratively. This iterative procedure is prone to destabilization, lack of convergence, and loss of precision [36]. (ii) A direct fit would not take advantage of the periodicity in time of the bound probability density that originates in beating vibrational components while Fourier transformation reveals time-periodic structures efficiently.

Continuing with the investigation of the Fourier-transformed probability density, we note that for large sampling times T , satisfying the condition (16), individual beat terms $\tilde{d}_{\nu,\mu}(R, \omega; T)$ in the R -dependent spectrum (12) do not overlap, such that the power spectrum simplifies to the incoherent sum

$$|\tilde{d}(R, \omega; T)|^2 = \sum_{\mu,\nu} |\tilde{d}_{\mu,\nu}(R, \omega; T)|^2. \quad (18)$$

The reconstruction of the amplitudes is then conveniently carried out with the help of the definitions

$$\begin{aligned} F(\omega)^{(k)} &\equiv \int_0^{\infty} dRR^k |\tilde{d}(R, \omega; T)|^2 \\ &= 2\pi |a_{\nu}|^2 |a_{\mu}|^2 |\delta_T(\Delta\omega_{\nu,\mu} - \omega)|^2 R_{\nu,\mu}^{(k)} \equiv I_{\nu,\mu}^{(k)}, \end{aligned} \quad (19)$$

$$R_{\nu,\mu}^{(k)} \equiv \int_0^{\infty} dRR^k |\chi_{\nu}^*(R)\chi_{\mu}(R)|^2, \quad (20)$$

$$\bar{I}_{\nu,\mu}^{(k)} \equiv \frac{1}{2\eta} \int_{\Delta\omega_{\nu,\mu}-\eta/2}^{\Delta\omega_{\nu,\mu}+\eta/2} d\omega I_{\nu,\mu}^{(k)}, \quad (21)$$

$$= 2\pi |a_{\nu}|^2 |a_{\mu}|^2 R_{\nu,\mu}^{(k)} D_{\nu,\mu}(\eta), \quad (22)$$

and

$$\begin{aligned} D_{\nu,\mu}(\eta) &\equiv \frac{1}{2\eta} \int_{\Delta\omega_{\nu,\mu}-\eta/2}^{\Delta\omega_{\nu,\mu}+\eta/2} d\omega |\delta_T(\Delta\omega_{\nu,\mu} - \omega)|^2 \\ &= \frac{\cos\left(\frac{\eta T}{2}\right) - 1}{\eta^2 \pi^2} + \frac{T}{2\eta\pi^2} \text{Si}\left(\frac{\eta T}{2}\right). \end{aligned} \quad (23)$$

Note that due to (i) our assumption of a sampling time that is large enough to satisfy Eq. (16), i.e., large enough to fully resolve the beat spectrum and (ii) the anharmonicity of the ground-state adiabatic potential curve of D_2^+ (that results in nonequal $\Delta\omega_{\nu,\nu+\Delta\nu}$ within a given $\Delta\nu$ series), only one term of the sum (18) contributes to Eq. (19) at any given beat frequency ω . The parameter η in the frequency average $\bar{I}_{\nu,\mu}^{(k)}$ is determined by the experimental frequency resolution and needs to be smaller or equal than the level spacings. The overlap integral $R_{\nu,\mu}^{(k)}$ can be calculated from the numerically known vibrational D_2^+ wave functions. The integrals $D_{\nu,\mu}(\eta)$ are known analytically, in terms of the sine-integral function $\text{Si}(x) \equiv \int_0^x dx \sin x/x$.

With these definitions, the recipe for the reconstruction of the amplitudes $\{|a_{\nu}|, \nu=1 \dots N\}$ consists of the following steps: (i) measure the KER spectrum as a function of the pump-probe delay by CE imaging, (ii) derive the time-delay-dependent nuclear probability density $d(R, t)$ from the KER spectrum, (iii) for a given sampling time interval T of time delays, Fourier transform $d(R, t)$ to obtain $\tilde{d}(R, \omega; T)$, (iv) compute $\bar{I}_{\nu,\mu}^{(k)}$ from $\tilde{d}(R, \omega; T)$ and $R_{\nu,\mu}^{(k)}$ from the numerically known vibrational eigenstates $\{\chi_{\nu}\}$, in order to obtain the set of real and positive numbers

$$K_{\nu,\mu}^{(k)} \equiv \frac{\bar{I}_{\nu,\mu}^{(k)}}{2\pi R_{\nu,\mu}^{(k)} D_{\nu,\mu}(\eta)}, \quad (24)$$

(v) solve the system of equations

$$|a_{\nu}|^2 |a_{\mu}|^2 = K_{\nu,\mu}^{(k)}. \quad (25)$$

The amplitude reconstruction can be performed based on any $k \geq 0$ —moment $R_{\nu,\mu}^{(k)}$. The exact reconstruction of the amplitudes does not depend on k . Thus, performing the amplitude reconstruction separately for several orders k , the dependence of the reconstructed amplitudes on k is indicative for the achieved accuracy. Obviously, the larger k is, the more emphasis is put on large R , i.e., on small values of the KER, and vice versa. This leaves some flexibility for adjusting the amplitude reconstruction to the finite range in KER (that is R) values that are accurately measured [37]. The preferred value of k emphasizes the range in internuclear distances R that are most accurately extracted by CE mapping from the

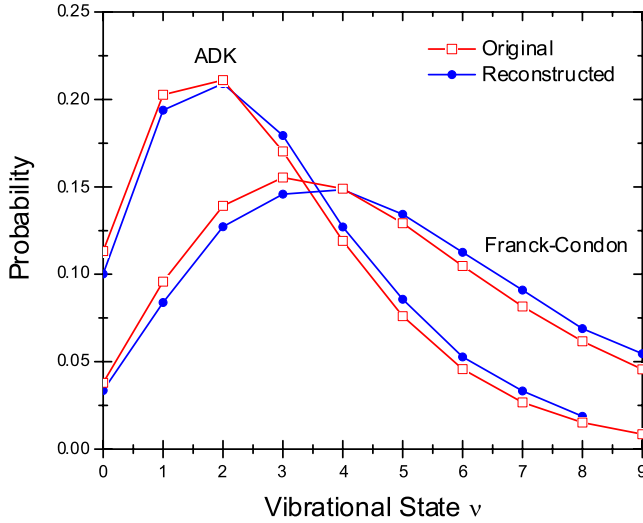


FIG. 4. (Color online) Original (squares) and reconstructed (dots) vibrational distribution $\{|a_\nu|^2\}$ for Franck-Condon and ADK-modified initial states of D_2^+ for a sampling time of 3 ps. The initial ADK distribution, is based on a 10^{14} W/cm², 800 nm, 6 fs Gaussian pump pulse.

measured KER. Instead of simply using a power of the internuclear distance R^k as weight factor in the definition (20), the amplitudes can also be reconstructed for more physically motivated weight factors such as, e.g., the molecular ADK rate for the ionization of the molecular ion.

In practise a subset of either $N-1$ or N equations of the system of N^2 Eqs. (25) will be selected, depending on whether dissociation occurs or not, respectively. If dissociation can be neglected, one additional equation is provided by the conservation of the wave-packet norm $\sum_\nu |a_\nu|^2 = 1$. A guide for the appropriate selection of a subset of equations is given by the magnitude of the numbers $K_{\nu,\mu}^{(k)}$ that is related to the experimental count rate. Equations with the largest right-hand sides $K_{\nu,\mu}^{(k)}$ are expected to be the best choice, leading to the most accurate reconstruction of $\{|a_\nu|, \nu = 1, \dots, N\}$.

For our numerical example, we chose the frequency-resolution parameter η equal to the average spacing between the relevant neighboring beat frequencies within the $\Delta\nu=1$ series. The area under a peak in Fig. 3(a) that is centered at $\Delta\omega_{\nu,\mu}$ is given by $\bar{I}_{\nu,\mu}^{(k)}$ (22). In order to reconstruct the wave packet amplitudes from the simulated R -dependent power spectrum in Fig. 3, we chose the lowest moment ($k=0$) in Eqs. (20) and (22). We then calculated $R_{\nu,\nu+1}^{(0)}$, $\bar{I}_{\nu,\nu+1}^{(0)}$, and $K_{\nu,\nu+1}^{(0)}$, in order to set up the system of Eqs. (25). Since the wave packet is freely evolving after the pump pulse, no dissociation occurs, and it is convenient to supplement Eq. (25) with the completeness relation $\sum_\nu |a_\nu|^2 = 1$. Numerical results for the reconstructed amplitudes are shown in Fig. 4 for both FC and ADK initial D_2^+ wave packets. For the generation of the D_2^+ ADK-wave packet in the first ionization step, a pump-pulse intensity of 10^{14} W/cm² and length of 6 fs was assumed. The sampling time in this calculation was $T=3$ ps. The reconstructed and exact stationary vibrational-state distributions agree well. Clearly, distributions that are based on molecular ADK rates are colder than the FC distri-

bution, in agreement with both, theory and the experiment of Urbain *et al.* [30]. It is worth to point out, however, that the distributions of Urbain *et al.* were generated by comparatively long 45 fs, 800 nm, 10^{14} W/cm² pump pulses and are slightly colder than our 6 fs-pump-pulse ADK distribution.

Small discrepancies between the reconstructed and exact distributions in Fig. 4 are due to the finite sampling time and inaccuracies in the computation of $R_{\nu,\nu+1}^{(0)}$ and $\bar{I}_{\nu,\nu+1}^{(0)}$. These small systematic errors are introduced by small overlaps of neighboring quantum beat peaks, the numerical integration over R , and frequency-averaging over individual peaks in Fig. 3(a). In corresponding experiments [23] these errors can be systematically reduced by (i) decreasing the time intervals between successive delay times, (ii) increasing the sampling time T , and (iii) increasing the energy resolution in the measured KER. We point out that the reconstruction examples in Fig. 4 are based on error-free, calculated probability densities rather than “real-life” data (measured KER spectra). Nevertheless, not accounting for noise in our simulations, we expect that existing experimental techniques, despite unavoidable noise and distortions in measured KER spectra, would still allow the determination of the stationary vibrational-state distribution in D_2^+ immediately after the rapid ionization of the neutral parent molecule in an ultra-short and intense laser pulse.

The discussed scheme for the amplitude reconstruction requires knowledge of the stationary vibrational states $\{\chi_\nu\}$. For small diatomic molecules, such as H_2^+ and their isotopes, accurate ground-state adiabatic electronic potential curves are available for the numerical calculation of all but the very weakly bound vibrational eigenstates. We note that for larger molecules, the stationary vibrational wave functions are in general not (accurately) known.

5. Phase reconstruction

The full characterization of the wave packet (1) (apart from an arbitrary overall phase factor) requires knowledge of the complex phases $\{\phi_\nu, \nu = 1, \dots, N\}$ of all—but one—of the expansion coefficients $\{a_\nu = |a_\nu|e^{i\phi_\nu}, \nu = 1, \dots, N\}$. For sufficiently large sampling times, that is, if T satisfies Eq. (16), the moment of order k of the nuclear probability density $\tilde{d}(R, \omega; T)$ defined by

$$J_{\nu,\mu}^{(k)} \equiv \int_0^\infty dRR^k \tilde{d}(R, \omega; T) \quad (26)$$

simplifies to

$$J_{\nu,\mu}^{(k)} \equiv \int_0^\infty dRR^k \tilde{d}_{\nu,\mu}(R, \omega; T). \quad (27)$$

Similar to the procedure in the preceding subsection, frequency averaging over a small frequency interval η leads to the definitions and results

$$\bar{J}_{\nu,\mu}^{(k)} \equiv \frac{1}{2\eta} \int_{\Delta\omega_{\nu,\mu}-\eta/2}^{\Delta\omega_{\nu,\mu}+\eta/2} d\omega J_{\nu,\mu}^{(k)}, \quad (28)$$

$$= \sqrt{2\pi} a_{\nu,\mu}^* a_{\nu,\mu} S_{\nu,\mu}^{(k)} \Theta_{\nu,\mu}(\eta), \quad (29)$$

$$S_{\nu,\mu}^{(k)} \equiv \int dR R^k \chi_{\nu}(R)^* \chi_{\mu}(R), \quad (30)$$

and

$$\Theta_{\nu,\mu}(\eta) \equiv \frac{1}{2\eta} \int_{\Delta\omega_{\nu,\mu}-\eta/2}^{\Delta\omega_{\nu,\mu}+\eta/2} d\omega \delta_T(\Delta\omega_{\nu,\mu} - \omega) = \frac{1}{2\pi\eta} \text{Si}\left(\frac{\eta T}{2}\right). \quad (31)$$

As for the amplitude reconstruction, η is determined by the experimental frequency resolution and needs to be smaller than all relevant level spacings. The integrals $S_{\nu,\mu}^{(k)}$ and $\Theta_{\nu,\mu}(\eta)$ are known numerically and analytically, respectively. Note that $J_{\nu,\mu}^{(0)} \sim \delta_{\nu,\mu}$, due to the orthogonality of the vibrational wave functions. Thus, in contrast to the amplitude reconstruction, the $k=0$ moment cannot be used for the phase reconstruction. The phase reconstruction can be performed based on any $k>0$ —moment $J_{\nu,\mu}^{(k)}$. As for the amplitude reconstruction, the preferred value for k depends on the range in internuclear distances R that are most conveniently extracted from the measured KER by Coulomb explosion mapping. Note further, that all wave functions $\chi_{\nu}(R)$, and thus $S_{\nu,\mu}^{(k)}$, can be assumed to be real valued.

In analogy to the amplitude reconstruction, a recipe for the reconstruction of the phase information in the superposition (1) is now easily compiled. Steps (i)–(iii), leading to the compilation of $\tilde{d}(R, \omega; T)$ from the KER spectrum, are identical and will not be repeated: (iv) compute $\bar{J}_{\nu,\mu}^{(k)}$ from $\tilde{d}(R, \omega; T)$ and $S_{\nu,\mu}^{(k)}$ from the numerically known vibrational eigenstates $\{\chi_{\nu}\}$, in order to obtain the set of complex numbers

$$L_{\nu,\mu}^{(k)} \equiv \frac{\bar{J}_{\nu,\mu}^{(k)}}{\sqrt{2\pi S_{\nu,\mu}^{(k)} \Theta_{\nu,\mu}(\eta)}} \quad (32)$$

and (v) solve the system of equations

$$a_{\nu}^* a_{\mu} = L_{\nu,\mu}^{(k)}. \quad (33)$$

At this point several strategies can be applied in order to extract all complex expansion coefficients $\{a_{\nu}, \nu=1, \dots, N\}$. Assuming that the amplitudes $\{|a_{\nu}|, \nu=1, \dots, N\}$ have already been reconstructed, Eq. (33) is best rewritten as

$$|a_{\nu}| |a_{\mu}| e^{i(\phi_{\nu} - \phi_{\mu})} = L_{\nu,\mu}^{(k)}, \quad (34)$$

which, since $\Theta_{\nu,\mu}(\eta) > 0$, implies that

$$\phi_{\nu} - \phi_{\mu} = \pm \arg \bar{J}_{\nu,\mu}^{(k)} \quad \text{for} \quad \mp S_{\nu,\mu}^{(k)} > 0, \quad (35)$$

where “arg” designates the argument of a complex number. Since the exact reconstruction of the phases does not depend on k , the dependence of the reconstructed phases on k is indicative for the achieved accuracy.

An alternative strategy for reconstructing the initial wave packet (1) consist in selecting a total number of $2N-1$ equations from the set of amplitude and phase reconstruction equations (25) and (33), and the normalization condition in order to determine all N complex expansion coefficients up to one overall phase factor. We note that knowledge of the stationary vibrational states in principle would also allow for

the reconstruction of amplitudes (and all relative phases) by least-square fitting the time- and R -dependent probability density. However, this fit would be difficult to perform in practice and less accurate than the procedure we suggest. The advantage of the suggested phase- and amplitude-reconstruction scheme is that it relies on a Fourier analysis which efficiently extracts the harmonics constituents given at the vibrational beat frequencies.

B. Dissociation

1. R -dependent Fourier analysis

The time-dependent nuclear probability density $d(r, t)$ images the dissociating part of the wave packet as jetlike structures that extend to large R within a short time near the peak values of the oscillating laser-electric force, while the delay-dependent KER spectrum shows dissociation as monotonically decreasing energy releases for increasing delay times [6,10,28]. While we focused in Sec. II A on bound nuclear motion in the D_2^+ molecule, we now turn our attention to dissociation which, strongly dependent on the intensity and shape of pump and probe laser pulses, will distort the time evolution of the bound wave packet to a variable degree. Allowing for dissociation, we generalize Eq. (1) by including continuum states χ_E of energy E of D_2^+ ,

$$\psi(R, t) = \sum_{\nu=0}^N a_{\nu} e^{-i\omega_{\nu} t} \chi_{\nu}(R) + \int_0^{\infty} dE a_E e^{-iEt} \chi_E(R). \quad (36)$$

Including continuum states, the harmonic analysis of ψ yields two distinct terms in addition to Eq. (12). In the limit of large sampling times ($T \rightarrow \infty$) we find

$$d(R, \omega; \infty) = \sqrt{2\pi} \left\{ \sum_{\nu,\mu=0}^N a_{\nu}^* a_{\mu} \chi_{\nu}^*(R) \chi_{\mu}(R) \delta(\Delta\omega_{\nu,\mu} - \omega) + \sum_{\nu=0}^N \int_0^{\infty} dE \chi_{\nu}^*(R) \chi_E(R) [a_{\nu}^* a_E \delta(\omega_{\nu} - E - \omega) + a_E^* a_{\nu} \delta(E - \omega_{\nu} - \omega)] + \int_0^{\infty} dE dE' a_E^* a_{E'} \chi_E^*(R) \chi_{E'}(R) \delta(E - E' - \omega) \right\}. \quad (37)$$

The last term is diffuse in R and ω and appears as a background at larger internuclear distances in $d(R, \omega; \infty)$. The second term is less diffuse in ω than the third term and may map some of the nodal structure of higher excited bound vibrational states.

2. Bond-hardened and bond-softened states

Laser-induced molecular dissociation and transiently trapped molecular states, such as bond-softening (BS) [2,18,19,38–40], bond-hardening (BH) [2,20,21,39–41], or above threshold dissociation [17,42], are often and conveniently explained within the Floquet picture [43] in terms of (laser-electric-field-) dressed molecular potential curves. For

sufficiently long and intense laser pulses, transiently trapped states may exist in the shallow well of a dressed potential curve of a molecule or molecular ion [20,23]. For a diatomic molecule, we expect the nodes of vibrational-state contributions to these “bond-hardened” states to emerge most distinctively in the $\Delta\nu=1$ series in $\tilde{d}(R, \omega; T)$ at larger values of R . Compared to the vibrational-state contributions of a bound nuclear wave packet, transient bond-hardened states are expected to appear fainter and somewhat blurred near $\omega = \Delta\omega_{\nu, \nu+1}$, due to dissociation. As one might expect, for the ultrashort pump pulses and the free wave-packet propagation underlying the results shown in Figs. 2 and 3, we find no evidence for bond-hardened states.

Our goal in this subsection is to illustrate that the R -dependent Fourier analysis introduced in Sec. II A is also suitable for observing dynamical characteristics of a moving wave packet that is exposed to a laser field. Our numerical simulations in Sec. II have illustrated this method for the imaging of the ground-state molecular potential curve of D_2^+ . Here the question arises, under which conditions dynamic features such as dressed, bond-hardened and -softened states emerge and how clearly they can be analyzed with the help of our R -dependent Fourier transformation-imaging scheme.

An intuitive answer might be that they do not emerge at all in fs laser pulses since the Floquet approach is based on the periodicity of the laser-electric field and thus restricted to comparatively long pulses, while highly resolved R -dependent Fourier imaging requests pump and probe pulses that are short on the time scale of the nuclear motion. However, the addition of a comparatively weak and long “background” intensity profile may allow these states to evolve such that dressed potential curves can be imaged. Following up on this speculation, we note that ultrashort few-fs pulses produced in the laboratory appear to sit on rather long pedestals. These pedestals are typically around 100 fs long at 5% of the peak intensity for 7 fs laser pulses [10,37,44]. They are long enough to validate the Floquet picture during the motion of the nuclear wave packet between the fs pump pulse and the leading edge of the fs probe pulse, weak enough to prevent severe dissociative losses, but strong enough to lead to a noticeable distortion (dressing) of field-free potential curves.

In order to illustrate the mapping of the nuclear dynamics in dressed potentials, we numerically investigated the influence of a pedestal at the probe pulse in wave-packet-propagation simulations. Figure 5(a) shows our results for 50 fs, 800 nm, 5×10^{13} W/cm² Gaussian pedestals. The pedestal is centered at the probe pulse. This means that the vibrational wave packet is propagated through the first half of the probe-pulse pedestal up to the given pump-probe delay immediately preceding the probe step. Performing many separate propagation calculations for pump-probe delay times between 0 and T , we obtained the time series $d(R, t)$ and Fourier transformed it. The actual shape of the fs probe pulse is not included. We thus implicitly assume an ideal probe pulse that instantaneously ionizes the molecular ion, without further distorting its vibrational-state distribution and attribute any change of the vibrational distribution by the

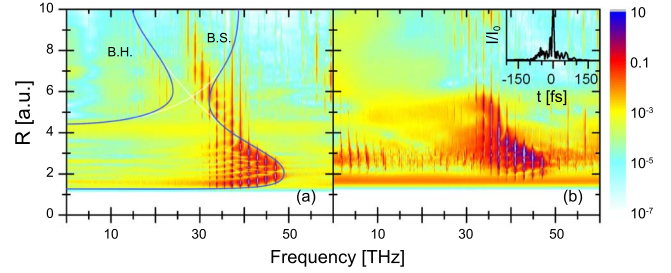


FIG. 5. (Color online) Power spectrum as a function of the frequency f and the internuclear distance R . (a) Propagation of an initial Franck-Condon wave packet with the inclusion of a 5×10^{13} W/cm², 50 fs [full width at half maximum (FWHM)] pedestal at the probe pulse causing “bond hardening” (BH) and “bond softening” (BS). The wave packet is sampled at the center of the probe pedestal. (b) Initial ADK-populated wave packet after a Gaussian 3×10^{14} W/cm², 6 fs pump pulse. The pedestal of a measured laser pulse profile (inset) is added for the propagation during the remainder of the pump pulse and preceding the Coulomb explosion by the probe pulse. Both graphs show the beat frequency $f = \omega / (2\pi)$ along the horizontal axis.

probe process solely to the leading half of the probe-pulse pedestal. For simplicity and in order to have higher vibrational states populated, an initial FC distribution is assumed.

Compared to the field-free propagation of the initial FC wave packet [see Fig. 3(c)] Fig. 5(a) shows several interesting features. A significant part of the nuclear probability density of the wave packet appears in the classically forbidden region at large R for frequencies between $f \approx 30$ and 40 THz. In addition, trapped states emerge at $R \approx 6$ near 20 THz. In the Floquet picture [42], the field-free $1s\sigma_g$ and the photon-energy shifted $2p\sigma_u$ potential curves combine to form the field-dressed adiabatic potential curves. These dressed potential curves enable BS and BH and correspond to the dark contour lines indicated in Fig. 5(a), while the diabatic dressed potential curve is represented by the white contour line (see Sec. II A 3 for the correspondence between contour lines in the quantum beat spectrum and potential curves). BS is responsible for the dissociation of the higher vibrational states, and is imaged in Fig. 5(a) as vertical lines that extend to large internuclear separations in the avoided crossing region. As the electric field increases during the pulse, the gap between the adiabatic potential curves increases and allows for the over-the-barrier dissociation and tunnel ionization of lower vibrational states. The figure maps the lowest light-induced potential well and shows a second light-induced potential well that causes the transient trapping of a small part of the nuclear probability density, i.e., BH.

The shape of short laser pulses can be determined using the Spectral Phase Interferometry for Direct Electric-field Reconstruction (SPIDER) technique [45]. The SPIDER-analyzed intensity profile of the pulses used in the experiment [23] shown in the inset of Fig. 2(a) is reproduced in the inset of Fig. 5(b). It exhibits a pedestal of approximately 100 fs length as well as a pronounced prepulse before the main peak. We started the wave-packet propagation calculations in Fig. 5(b) with an initial ADK wave packet in D_2^+ that was provided by a 6 fs Gaussian pump pulse with a peak inten-

sities of 3×10^{14} W/cm². The wave packet was subsequently propagated through the second half of the measured SPIDER pulse profile, starting at time $t=0$. Immediately preceding the probe-pulse-delay time it was propagated under the influence of the first half of the SPIDER pulse. The Coulomb explosion of D_2^+ from the $1s\sigma_g$ and $2p\sigma_u$ channels during the probe pulse is modeled by (i) the R -dependent molecular ADK rates $\Gamma_g^{D_2^+}[R, E(t)]$ and $\Gamma_u^{D_2^+}[R, E(t)]$ and by (ii) incoherently adding the probabilities for ionization out of these two channels

$$\rho_{CE}(R) = \int_{-\infty}^{\infty} (1 - e^{-\Gamma_g^{D_2^+}[R, E(t)]t}) |\chi_g(R, t)|^2 dt + \int_{-\infty}^{\infty} (1 - e^{-\Gamma_u^{D_2^+}[R, E(t)]t}) |\chi_u(R, t)|^2 dt. \quad (38)$$

In this model (and throughout this paper) we neglect the kinetic energy of the wave packet at the time of the ionization, but include the R -dependent ionization rates leading to the Coulomb explosion. The spectrum agrees reasonably well with the experimental data shown in the inset of Fig. 2(b). The vertical lines between $f=30$ and 40 THz extending to large R are caused by dissociation in the SPIDER-pulse pedestal, while no evidence is found for the occurrence of bond hardening states at the given laser parameters. The nodal structure disappears, even for the lowest bound vibrational states.

3. Pulse length and intensity dependence of bond softening and hardening

While the proposed R -dependent imaging method is general and can, in principle, be applied to any kind of electronic or nuclear dynamics, it may be employed to question the physical significance of dressed states and the validity of the Floquet interpretation as a function of the laser pulse lengths and intensities. With this in mind, we carried out a series of simulations in which the lengths and intensities of the probe-pulse pedestals were varied. The propagation calculations were performed for Gaussian pedestals and provide the quantum-beat spectrum that an ideal superimposed probe pulse would detect. The probe pulse is thus assumed to instantaneously ionize the molecular ion. As in the previous subsection, only the leading half of the probe-pulse pedestal, not the probe pulse itself, is included in the simulations, i.e., we propagated the molecular wave function up to the peak intensity of the pedestal. As for the results shown in Fig. 5(a), no pump-pulse pedestal is included.

The graphs in Fig. 6 are ordered as a matrix with pedestal intensities increasing from 5×10^{12} W/cm² (top row) to 10^{14} W/cm² (bottom row). The pedestal lengths (FWHM) are 20 fs (first column) and 50 fs (second column). The third column shows the limit of long probe pedestals (cw). The cw pulses were turned on over 10 optical cycles with a sine-squared envelope function immediately after the pump step. The color coding is the same for all graphs and extends over 10 orders of magnitude. BS appears as vertical stripes that “shoot out” of the undisturbed $\Delta\nu=1$ —beat spectrum of the lowest adiabatic potential curve. For higher peak intensities

of the probe-pulse pedestal, BS depletes the highest vibrational levels which tends to prevent the population of BH states.

For a pedestal length of 50 fs and pedestal intensities up to 5×10^{13} W/cm², BS across the $1-\omega$ barrier and BH in the $1-\omega$ BH well are easily visible in Fig. 6. The $1-\omega$ BH states appear at frequencies below 25 THz at internuclear distances between approximately 4 and 8. At the two highest intensities, dissociation across the $3-\omega$ barrier and weak evidence for BH in the $3-\omega$ BH well of the dressed D_2^+ adiabatic Floquet potential are imaged. At the highest shown intensity (10^{14} W/cm²) and for 50 fs probe pedestals, all higher lying vibrational states are removed by BS before the peak intensity of the probe pulse pedestal is reached, and BH at the $1-\omega$ crossing has completely disappeared.

We note that BS appears as probability density outside the classically allowed regime of the laser-field-free potential in the two left columns of Fig. 6 [and also in Fig. 5(a)]. This is due to intensity averaging in the following sense. Since a sampling time of 10 ps was used in Fig. 6, by far most time delays are long enough for the molecular wave packet to propagate freely most of the time. This leads to the imaging of (part of) the field-free ground-state molecular potential curves in the two left columns of Fig. 6. However, immediately before the probe pulse destroys the molecular ion, it evolves through the probe-pulse pedestal and dissociates into the $1-\omega$ channel at lower intensities and into the $1-\omega$ and $3(2)-\omega$ channels at the highest shown pedestal intensities. Thus, since the Fourier analysis integrates over both, free propagation and propagation with BS in the probe-pulse pedestal, BS in Figs. 6 and 5(a) is mapped with superimposed free-propagation characteristics, i.e., in the classically forbidden region of the laser-field-free potential curve.

In the long pulse limit, for cw probe pedestals, the widening of the field-dressed $1s\sigma_g$ molecular potential curve with increasing laser intensity explains the shift toward lower beat frequencies in Fig. 6. Due to the comparatively large pulse energy, BH states do not appear. As for the finite-length pulses, dissociation by BS depletes the bound vibrational-states distribution from above. However, BS does not appear as vertical stripes in the power spectra, as one might expect, since it happens early on in the cw pulse and, in the average over the entire time series, long before the end of the propagation interval.

III. DECOHERENCE

The time-series analysis of KER data can be extended and used in order to quantify the degree of coherence in a nuclear vibrational wave packet. With this goal in mind, we extend our analysis by allowing for both, coherent and incoherent mixtures $\{p_\nu, \chi_\nu\}$ of bound vibrationally excited states. For the clarity of the presentation only, we do not include continuum states $\{\chi_E(R)\}$ of the molecular ion in this section. The numbers $p_\nu = |a_\nu|^2$ represent the probabilities for finding a given stationary vibrational state χ_ν in the statistical mixture. The corresponding density operator

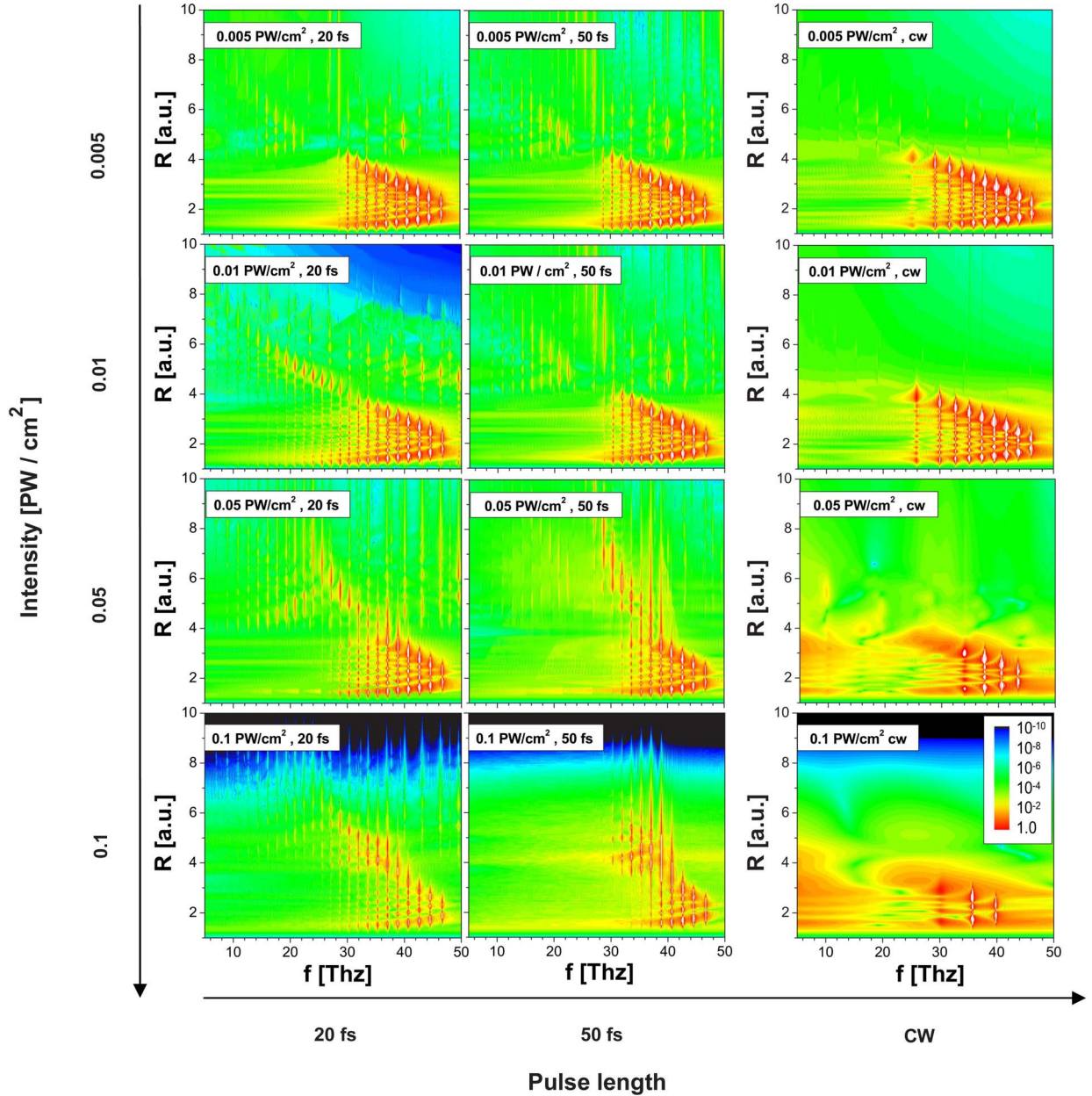


FIG. 6. (Color online) Power spectra as a function of the frequency f and the internuclear distance R . Propagation of an initial Franck-Condon wave packet for probe-pulse pedestals with peak intensities of 5×10^{12} W/cm 2 , 10^{13} W/cm 2 , 5×10^{13} W/cm 2 , and 10^{14} W/cm 2 and pulse lengths (FWHM) of 20 and 50 fs. The third column shows results for cw pulses that are turned on with a \sin^2 raise over ten laser cycles immediately after the pump step. The wave packet is sampled at the center of the probe pedestal. The sampling time is 10 ps. All graphs are plotted with the same logarithmic color scale. 1 PW is equal to 10^{15} W/cm 2 .

$$\rho_{v,\mu}^{\text{inc}} = \sum_{\nu=0}^N p_{\nu} |\chi_{\nu}\rangle \langle \chi_{\nu}| \quad (39)$$

is represented by the diagonal matrix $\rho_{v,\mu}^{\text{inc}} = p_{\nu} \delta_{\nu,\mu}$ relative to the basis $\{\chi_{\nu}\}$. Without external interactions, $\rho_{v,\mu}^{\text{inc}}$ is time independent. Denoting the time-dependent density matrix of the pure state (1) as $\rho^{\text{coh}}(t) = |\Psi(t)\rangle \langle \Psi(t)|$ results in the relation

$$\rho_{v,\mu}^{\text{coh}} = a_{\nu}^* a_{\mu} e^{-i\Delta\omega_{\nu,\mu}t} = \rho_{v,\mu}^{\text{inc}} + \rho_{v,\mu}^{\text{coh}}(1 - \delta_{\nu,\mu}). \quad (40)$$

In contrast to $\rho_{v,\mu}^{\text{inc}}$, $\rho_{v,\mu}^{\text{coh}}$ is not diagonal in the $\{\chi_{\nu}\}$ basis and includes time-dependent off-diagonal elements. The degree

of (de)coherence is given by the relative importance of these off-diagonal elements.

In terms of density matrix elements, the probability density can be written as

$$|\Psi(R,t)|^2 = D^{\text{inc}}(R) + d(R,t), \quad (41)$$

with the time-independent incoherent contribution

$$D^{\text{inc}} \equiv \sum_{\nu} \rho_{\nu,\nu} |\chi_{\nu}(R)|^2. \quad (42)$$

and, consistent with Eqs. (10) and (11), the coherent contribution

$$d(R, t) = \sum_{\nu \neq \mu} \rho_{\nu, \mu}^{\text{coh}}(t) \chi_{\nu}^*(R) \chi_{\mu}(R). \quad (43)$$

In the harmonic analysis the incoherent contribution D^{inc} at $\omega \approx 0$ is imaged as a diffuse background over the entire range of classically allowed internuclear distances and is subtracted in the definition $d(R, \omega; T)$ in Eq. (11).

The continuous loss of coherence of the vibrational wave packet due to weak randomly fluctuating external forces can be imaged as a sequence of finite-time Fourier transformations (12) for a series of increasing sampling times T_i . More specifically, by modeling decoherence in terms of an additional random phase factor in each expansion coefficient of the wave packet, i.e., by replacing the set of complex numbers $\{a_{\nu}\}$ that characterize the coherent wave packet by $\{a_{\nu}(t) \equiv a_{\nu} \exp(i\alpha_{\nu}(t))\}$ with random phases $\alpha_{\nu}(t)$, the harmonic analysis of Eq. (41) for finite T results in

$$\begin{aligned} \tilde{d}(R, \omega; T) &= \frac{1}{\sqrt{2\pi}} \sum_{\nu \neq \mu} \chi_{\nu}^*(R) \chi_{\mu}(R) \\ &\times \int_0^T dt a_{\nu}^*(t) a_{\mu}(t) e^{i(\Delta\omega_{\nu, \mu} - \omega)t}. \end{aligned} \quad (44)$$

The coherent contributions in Eq. (41) disappear in the limit of very large time intervals $[0, T]$, such that for increasing sampling times lines in $\tilde{d}(R, \omega; T)$ at frequencies $\Delta\omega_{\nu, \mu} \neq 0$ eventually fade away. Thus, as T becomes much larger than the typical decoherence time T_d of the molecules in their environment, only the incoherent contribution D^{inc} to Eq. (41) remains, while

$$\tilde{d}(R, \omega; T \gg T_d) \rightarrow 0. \quad (45)$$

The time series of spectra $\{\tilde{d}(R, \omega, T_i) | T_1 < T_2 < \dots\}$, obtained by measuring the kinetic energy release over a range of pump-probe delays of the order of T_d constitutes a means to quantify the degree of (de)coherence in the nuclear motion. This is of possible interest to quantum information storage and quantum computing. As an integrated measure for the degree of decoherence, we suggest to relate the total coherent intensity

$$\bar{F} \equiv \int d\omega F(\omega)^{(k)} = \sum_{\nu \neq \mu} \bar{I}_{\nu, \mu}^{(k)} \quad (46)$$

to total incoherent contribution

$$\bar{D}^{\text{inc}} \equiv \int_0^{\infty} dR |D^{\text{inc}}(R)|^2. \quad (47)$$

The function $\eta^{\text{coh}}(T) \equiv \bar{F} / \bar{D}^{\text{inc}}$ then provides a measure for the progression of decoherence for increasing T . Clearly, for very large T , random-phase fluctuations imply that $\eta^{\text{coh}}(T) \rightarrow 0$.

IV. CONCLUSIONS

R -dependent Fourier transformation imaging has been applied to analyze the nuclear motion in D_2^+ . This imaging method displays the nodal structure of bound vibrational states of the lowest adiabatic potential curve of the molecular ion and the corresponding vibrational transition energies. Furthermore it offers the prospect of imaging laser-dressed molecular potential curves based on a time series of measured kinetic energy release spectra. Extensions of this method include (i) the full reconstruction of the initial wave packet and (ii) the quantitative analysis of the progression of decoherence in the nuclear motion due to couplings with the environment.

The imaging scheme proposed in this work is based on CE explosion mapping of the nuclear motion in molecules. As CE mapping requests instant ionization, one may be tempted to conclude that our analysis relies on ideal, ultrashort laser pulses in order to validate CE mapping. By including a relative long, low intensity pedestal in probe-pulse profile, our simulations indicate how a ‘‘real life’’ probe pulse may distort an ideal CE image.

At what level of accuracy field-free and field-dressed potential curves can be deduced from measured KER spectra as discussed in this work remains to be investigated in future experiments. First experiments [23] are encouraging.

ACKNOWLEDGMENTS

We are grateful to Artem Rudenko, Thorsten Ergler, and Robert Moshhammer for many stimulating discussions. We also thank Joachim Ullrich for his careful review of an early version of this manuscript and valuable suggestions. One of us (U.T.) acknowledges the hospitality of the Max-Planck Institute for Nuclear Physics in Heidelberg where part of this work was performed. This work was supported by the NSF and the Division of Chemical Sciences, Office of Basic Energy Sciences, Office of Energy Research, and U.S. DOE.

-
- [1] A. H. Zewail, *J. Phys. Chem. A* **104**, 5660 (2000).
 [2] J. H. Posthumus, *Rep. Prog. Phys.* **67**, 623 (2004).
 [3] I. V. Hertel and W. Radloff, *Rep. Prog. Phys.* **69**, 1897 (2006).
 [4] T. Brixner, G. Krampert, T. Pfeifer, R. Selle, G. Gerber, M. Wollenhaupt, O. Graefe, C. Horn, D. Liese, and T. Baumert, *Phys. Rev. Lett.* **92**, 208301 (2004).
 [5] A. S. Alnaser, X. M. Tong, T. Osipov, S. Voss, C. M. Maharjan, P. Ranitovic, B. Ulrich, B. Shan, Z. Chang, C. D. Lin, and

- C. L. Cocke, *Phys. Rev. Lett.* **93**, 183202 (2004).
 [6] A. S. Alnaser, B. Ulrich, X.M. Tong, I. V. Litvinyuk, C.M. Maharjan, P. Ranitovic, T. Osipov, R. Ali, S. Ghimire, Z. Chang, C.D. Lin, and C.L. Cocke, *Phys. Rev. A* **72**, 030702(R) (2005).
 [7] A. Bhattacharjee and K. R. Dastidar, *Phys. Rev. A* **72**, 023419 (2005).
 [8] T. Ergler, A. Rudenko, B. Feuerstein, K. Zrost, C. D. Schröter,

- R. Moshhammer, and J. Ullrich, Phys. Rev. Lett. **95**, 093001 (2005).
- [9] T. Ergler, B. Feuerstein, A. Rudenko, K. Zrost, C. D. Schröter, R. Moshhammer, and J. Ullrich, Phys. Rev. Lett. **97**, 103004 (2006).
- [10] A. Rudenko, T. Ergler, B. Feuerstein, K. Zrost, C. D. Schröter, R. Moshhammer, and J. Ullrich, Chem. Phys. **329**, 193 (2006).
- [11] H. Niikura, D. M. Villeneuve, and P. B. Corkum, Phys. Rev. A **73**, 021402(R) (2006).
- [12] J. H. Posthumus, J. Plumridge, P. F. Taday, J. H. Sanderson, A. J. Langley, K. Codling, and W. A. Bryan, J. Phys. B **32**, L93 (1999).
- [13] C. Trump, H. Rottke, and W. Sandner, Phys. Rev. A **59**, 2858 (1999).
- [14] S. Chelkovski and A. D. Bandrauk, Phys. Rev. A **65**, 023403 (2002).
- [15] B. Feuerstein and U. Thumm, Phys. Rev. A **67**, 043405 (2003).
- [16] B. Feuerstein and U. Thumm, Phys. Rev. A **67**, 063408 (2003).
- [17] A. Staudte, D. Pavićić, S. Chelkowski, D. Zeidler, M. Meckel, H. Niikura, M. Schöffler, S. Schössler, B. Ulrich, P. P. Rajeev, T. Weber, T. Jahnke, D. M. Villeneuve, A. D. Bandrauk, C. L. Cocke, P. B. Corkum, and R. Dörner, Phys. Rev. Lett. **98**, 073003 (2007).
- [18] A. D. Bandrauk and L. M. Sink, J. Chem. Phys. **74**, 1110 (1981).
- [19] P. H. Bucksbaum, A. Zavriyev, H. G. Muller, and D. W. Schumacher, Phys. Rev. Lett. **64**, 1883 (1990).
- [20] L. J. Frasinski, J. H. Posthumus, J. Plumridge, K. Codling, P. F. Taday, and A. J. Langley, Phys. Rev. Lett. **83**, 3625 (1999).
- [21] L. J. Frasinski, J. Plumridge, J. H. Posthumus, K. Codling, P. F. Taday, E. J. Divall, and A. J. Langley, Phys. Rev. Lett. **86**, 2541 (2001).
- [22] H. Schwöerer, P. Pausch, M. Heid, and W. Kiefer, Chem. Phys. Lett. **285**, 240 (1998).
- [23] B. Feuerstein, T. Ergler, A. Rudenko, K. Zrost, C. D. Schröter, R. Moshhammer, J. Ullrich, T. Niederhausen, and U. Thumm, Phys. Rev. Lett. **99**, 153002 (2007).
- [24] H. Niikura, D. M. Villeneuve, and P. B. Corkum, Phys. Rev. Lett. **92**, 133002 (2004).
- [25] D. S. Murphy, J. McKenna, C. R. Calvert, I. D. Williams, and J. F. McCann, New J. Phys. **9**, 260 (2007).
- [26] T. Niederhausen and U. Thumm, Phys. Rev. A **77**, 013407 (2008).
- [27] J. McKenna, W. A. Bryan, C. R. Calvert, E. M. L. English, J. Wood, D. S. Murphy, I. C. E. Turcu, J. M. Smith, K. G. Ertel, O. Chekhlov, E. J. Divali, J. F. McCann, W. R. Newell, and I. D. Williams, J. Mod. Opt. **54**, 1127 (2007).
- [28] T. Ergler, A. Rudenko, B. Feuerstein, K. Zrost, C. D. Schröter, R. Moshhammer, and J. Ullrich, Phys. Rev. Lett. **97**, 193001 (2006).
- [29] A. Saenz, J. Phys. B **33**, 4365 (2000).
- [30] X. Urbain, B. Fabre, E. M. Staicu-Casagrande, N. de Ruelle, V. M. Andrianarijaona, J. Jureta, J. H. Posthumus, A. Saenz, E. Baldit, and C. Cornaggia, Phys. Rev. Lett. **92**, 163004 (2004).
- [31] J. P. Brichta, W.-K. Liu, A. A. Zaidi, A. Trottier, and J. H. Sanderson, J. Phys. B **39**, 3769 (2006).
- [32] M. V. Ammosov, N. B. Delone, and V. P. Krainov, Zh. Eksp. Teor. Fiz. **91**, 2008 (1986); M. V. Ammosov, N. B. Delone, and V. P. Krainov, Sov. Phys. JETP **64**, 1191 (1986).
- [33] X. M. Tong, Z. X. Zhao, and C. D. Lin, Phys. Rev. A **66**, 033402 (2002).
- [34] D. R. Bates, K. Ledsham, and A. L. Stewart, Philos. Trans. R. Soc. London, Sect. A **246**, 215 (1953).
- [35] K. C. Kulander, F. H. Mies, and K. J. Schafer, Phys. Rev. A **53**, 2562 (1996).
- [36] W. H. Press, S. A. Teukolsky, W. T. Vetterling, and B. P. Flannery, *Numerical Recipes* (Cambridge University Press, Cambridge, England, 1992).
- [37] R. Moshhammer (private communication).
- [38] I. D. Williams, P. McKenna, B. Srigengan, I. M. G. Johnston, W. A. Bryan, J. H. Sanderson, A. El-Zein, T. R. J. Goodworth, W. R. Newell, P. F. Taday, and A. J. Langley, J. Phys. B **33**, 2743 (2000).
- [39] K. Sändig, H. Figger, and T. W. Hänsch, Phys. Rev. Lett. **85**, 4876 (2000).
- [40] H. Abou-Rachid, T. T. Nguyen-Dang, and O. Atabek, J. Chem. Phys. **114**, 2197 (2001).
- [41] A. Giusti-Suzor and F. H. Mies, Phys. Rev. Lett. **68**, 3869 (1992).
- [42] A. Giusti-Suzor, X. He, O. Atabek, and F. H. Mies, Phys. Rev. Lett. **64**, 515 (1990).
- [43] S. R. Barone, M. A. Narcowich, and F. J. Narcowich, Phys. Rev. A **15**, 1109 (1977).
- [44] F. Légaré and F. K. Lee, I. V. Litvinyuk, P. W. Dooley, A. D. Bandrauk, D. M. Villeneuve, and P. B. Corkum, Phys. Rev. A **72**, 052717 (2005).
- [45] C. Iaconis and A. Walmsley, Opt. Lett. **23**, 792 (1998).